Angular rate determination using star sensors and novel algorithms based on geometrical investigations

Dario Spiller[a,*], Fabio Curti[b]

[a] *PostDoc fellow*
[b] *Associate Professor*
School of Aerospace Engineering, Sapienza University of Rome, Via Salaria 851

Abstract

In this paper, a geometrical investigation of the star sensor image is performed under dynamic conditions where the angular velocity effects are non negligible. It is shown that, when the spacecraft is rotating, the streaks left by the stars' signal onto the star sensor detector belong to portions of conic sections which features depend on the angles between the instantaneous rotation axis, the sensor line of sight and the stars' direction. The geometrical properties discussed in the first part of the paper can be used to develop new numerical methods for the evaluation of the angular velocity. Hence, the chord method is proposed and discussed. This approach needs at least two stars in two successive images and, despite its simplicity, is quite effective to get a preliminary estimation of the spacecraft angular velocity in terms of direction and magnitude. The chord method is firstly presented by means of simple examples using some reference geometries, and then it is applied to real scenarios by using a high fidelity star sensor simulator. To this aim, the pre-processing and processing of simulated images are discussed, presenting some geometrical techniques allowing to correctly cluster the streaks. Results are presented and discussed, validating the reported theoretical speculations.

Keywords: Angular rate determination, star sensors, chord method.

*Corresponding author
Email addresses: dario.spiller@uniroma.it (Dario Spiller), fabio.curti@uniroma1.it (Fabio Curti)

1. Introduction

Angular rate determination represents an essential task for the navigation system of space platform [1]. Usually, the evaluation of the rate is demanded to gyroscopes [2], but new mission concepts have been recently proposed relying on different sensors. In [3], for instance, a magnetometer-only attitude and angular velocity filtering estimation is proposed. This paper will focus on the determination of the angular velocity from star sensor measurements.

Star sensors already represent the best technology concerning attitude determination [4], and their usage can be extended to rate determination. This new paradigm can help the on-board navigation system and eventually lead to avoid using gyroscopes and simplify the overall satellite hardware architecture. When the satellite experiences a non-negligible angular velocity, stars inside the sensor field of view (FOV) leave a trace which is no more a circular spot but an elongated streak. Even though the blurred star streaks can represent a problem to be considered for attitude determination, as reported for instance in [5], star streaks can be used to develop new algorithms for determining the angular velocity. Preliminary studies date back to the 80s, as the one reported in [6], where the open-loop performances of an attitude/attitude rate estimator based on a Kalman filter are discussed. Other studies appeared in the early 2000s, as in [7, 8] where an attitude rate dynamic estimator requiring the knowledge of the inertia tensor is proposed. In [9] the differential calculus and the rigid motion equations are used to identify the rotation that best fits the observed star trajectories in the sensor field of view. A finite-difference approach along with the least square technique is proposed in [10], whereas in [11] the star streak is studied as belonging to the circle on the celestial sphere. A simple linear Kalman filter approach is proposed in [12] for the estimation of incremental angle and angular rate from successive observations of a star tracker, without the use of star catalog or auxiliary sensors. Two different algorithms are presented for the estimation of spacecraft body angular rates in the absence of gyro rate data in [13]. In the first approach, body angular rates are estimated

with the spacecraft attitude using a dynamical model of the spacecraft. The second approach makes use of a rapid update rate of star camera to estimate the spacecraft body angular rates independent of spacecraft attitude. An algorithm based on the Wahba problem and using a differentiation approach without a spacecraft dynamics model is proposed in [14]. In recent years, some predominant techniques for the evaluation of the angular velocity from star sensors have been proposed, such as techniques based on optical-flow of stars discussed in [15, 16, 17, 18, 19, 20], techniques based on kalman-filtering approaches as the ones proposed in [21, 22, 23, 24], or even a combination of the two previous methods, as in [20].

In this paper, it is shown that the streaks are portions of conic sections when observed in the focal plane. Basing on some preliminary results and analysis reported in [25, 26], it is demonstrated that the intersection point of the rotation axis with the focal plane lies on the line passing through the conic section foci and the geometrical center of the detector. A mathematical model to simulate the generation of the conic section is developed and it is used to discuss theoretical investigations involving osculating circles near the vertex points, properties of the conic sections, and relationships between the previous two points and the angular velocity vector.

The discussed geometrical properties can be exploited to develop new methods for the evaluation of the angular rate in dynamical conditions without needing any attitude information. In the frame of this research, the angular velocity estimation is performed by means of the chord method, which is based on the computation of the normal to the streaks and their intersections. As a consequence, at least two streaks are required, and the proposed methodology can be used until two streaks are simultaneously available.

A high-fidelity simulator, already used in [27, 28], is used to generate synthetic images with the star streaks and all the fundamental noise sources due to electronics and space environment. The software environment is able to simulate broken streaks as the angular velocity increases, due to the fact that the energy of the star is spread on a bigger amount of pixel with respect to what

happens in the static case. Accordingly, specific algorithms for the clustering of the streaks and the recognition of same streaks in consecutive images are proposed. Preliminary results will be shown using this simulator, in order to prove the opportunities offered by the proposed geometric method. To summarize, the contributions of this paper are the following:

- Geometrical investigation of the relationships between conic sections and streaks left by stars' signal in dynamics conditions.
- Development of the chord method for the evaluation of the angular velocity direction.
- Description of image processing techniques to perform the clustering operation in dynamic conditions.
- Example application of the proposed method in a high fidelity star sensor simulator and discussion of the results.

The paper is organized as follows. In Sec. 2 the geometrical analysis of star streaks in dynamic conditions is performed and new theorems concerning the involved conics are developed. In Sec. 3 the algorithm for the determination of the angular velocity is described. Hence, the chord method is presented for the determination of the angular velocity direction. Sec. 4 is focused on the processing of the image coming from a high-fidelity star sensor simulator. This processing is required in order to get the information needed by the proposed chord method in real-case scenarios. Sec. 5 reports the numerical results with reference to a preliminary test case. Finally, Sec. 6 gives conclusions and final remarks.

A remark on notation: Through this paper, $\overline{AB}$ refers to the segment with endpoints A and B. AB, on the other hand, refers to the length of the segment with endpoints A and B. The symbol $\cong$ is used to mean that two geometrical quantities are congruent.

2. Geometrical analysis of star streaks in dynamic conditions

With reference to Fig. 1, the unit vector $\boldsymbol{u}$ pointing to a generic star within the FOV is defined in the sensor's reference frame $\mathcal{S} = \{\hat{\boldsymbol{x}}_{\mathcal{S}}, \hat{\boldsymbol{y}}_{\mathcal{S}}, \hat{\boldsymbol{z}}_{\mathcal{S}}\} \subset \mathbb{R}^3$, with origin in the focal point, and it is evaluated according to the pinhole camera model,

$$\boldsymbol{u} = \frac{1}{\sqrt{c_y^2 + c_z^2 + f^2}} \begin{bmatrix} f \\ -c_y \\ -c_z \end{bmatrix}, \tag{1}$$

where f is the focal length of the camera. The centroid position $\boldsymbol{c} = [c_y, c_z]^{\mathsf{T}}$ is

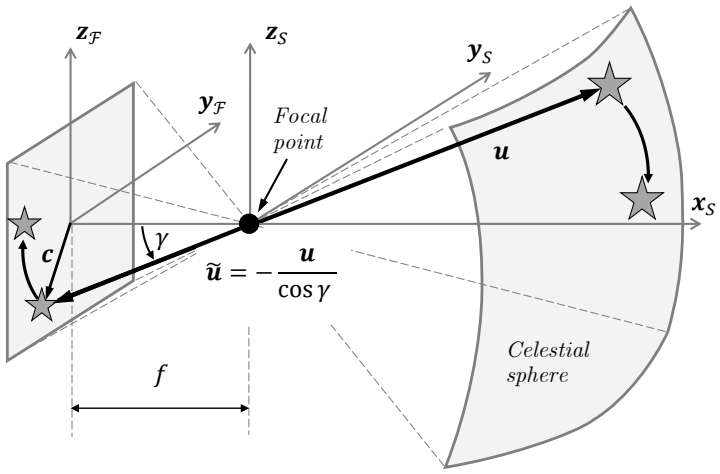

Figure 1: Sensor and focal plane reference frames.

defined in the two-dimensional focal reference frame $\mathcal{F} = \{\hat{\boldsymbol{y}}_{\mathcal{F}}, \hat{\boldsymbol{z}}_{\mathcal{F}}\} \subset \mathbb{R}^2$. The line of sight (LOS) corresponds to $\hat{\boldsymbol{x}}_{\mathcal{S}}$ and is perpendicular to the focal plane. The point reached by the unit vector $\boldsymbol{u}$ of the star tracker lies on a portion of the celestial sphere, which is assumed to be the sphere with unit radius that contains all the stars that can be seen by the star sensor. There are other more sophisticated models different from the simple pinhole camera one, given in Eq. (1) [29], but their application is beyond the scope of this work.

While $\boldsymbol{u}$ is a unit vector pointing far from the detector toward the celestial

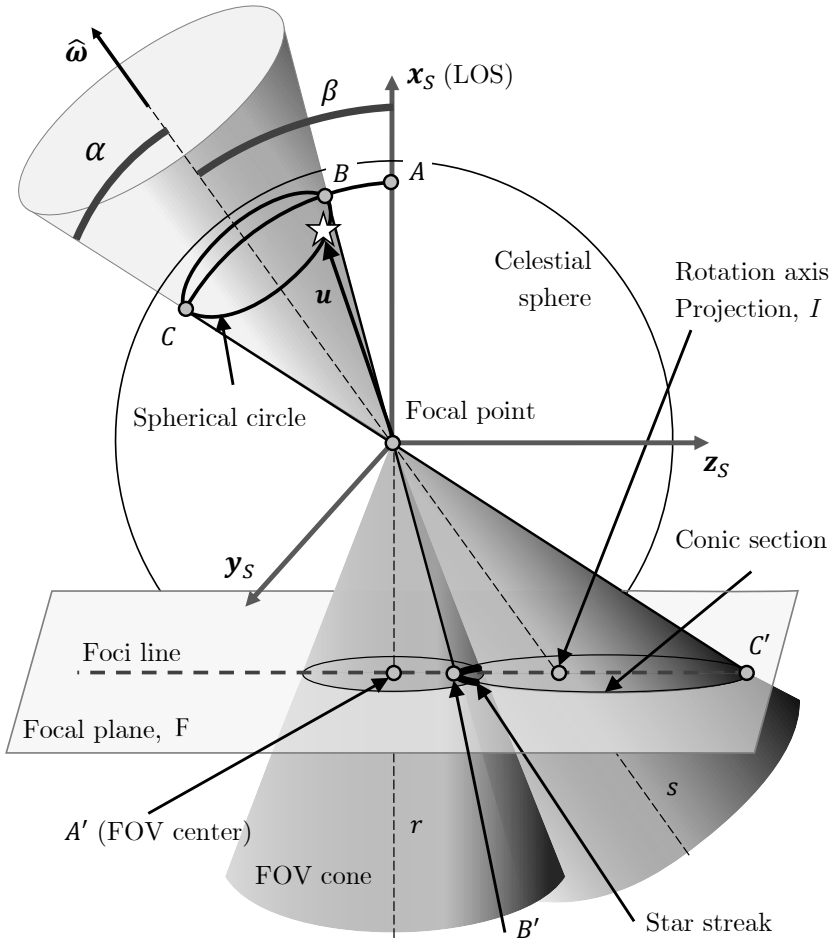

Figure 2: 3D representation of the studied geometry.

sphere, the vector $\tilde{\boldsymbol{u}}$ defined in Fig. 1 points to the position of the star in the detector starting from the focal point. This vector is evaluated as

$$\tilde{\boldsymbol{u}} = -\frac{\boldsymbol{u}}{\cos\gamma} \tag{2}$$

where γ is the angle between $\boldsymbol{u}$ and the LOS and will be used in the following for the determination of the angular rate.

In Fig. 2 the relationship between the star trajectory and the angular ve-

locity is depicted. The detector (which is not reported in the figure) lies inside the circle identified by the intersection of the FOV cone with the focal plane. With reference to Fig. 2, one can easily demonstrate the following results.

Theorem 1. *Let the angular velocity vector be constant, both in direction and magnitude, during the acquisition time interval. Then, star streaks in the focal plane belong to conic sections.*

Proof. The proof is trivial. Indeed, when the angular velocity is constant in direction and magnitude, the star (supposed to be at the extremity of the unit vector $\boldsymbol{u} \in \mathcal{S} \subset \mathbb{R}^3$) describes a trajectory belonging to a circle of the unitary celestial sphere. Such circle is given by the intersection between the celestial sphere and the cone spanned by the unit vector $\boldsymbol{u}$ while moving around $\hat{\boldsymbol{\omega}}$. On the other side of the focal point, the intersection between the cone and the image plane define a conic which features depend upon the angle β. ■

It is noteworthy that the result of the previous theorem remains valid no matter what the rotation around the line of sight is. This is why this further degree of freedom is not mentioned in the theorem. Indeed, a rotation around the LOS is directly related to a rotation of the conics in the focal plane.

Corollary. Under the hypothesis of Theorem 1, the foci line of the conic section contains the FOV center.

Proof. For the sake of simplicity (and without loss of generality), let the conic be an ellipse. With reference to Fig. 2, the vertex points B' and C' are the projections of the points B and C belonging to the circle of the celestial sphere. Among all the points belonging to this circle, B is the closest point to A and C is the farthest point from A. Hence, it can be seen quite easily that the points A, B, and C belong to the same great circle. The projection of this great circle onto the focal plane lies on the foci line. Hence, A' (i.e., the projection of A and the FOV center) belongs to the foci line. ■

As a consequence of the previous points, the following remark holds.

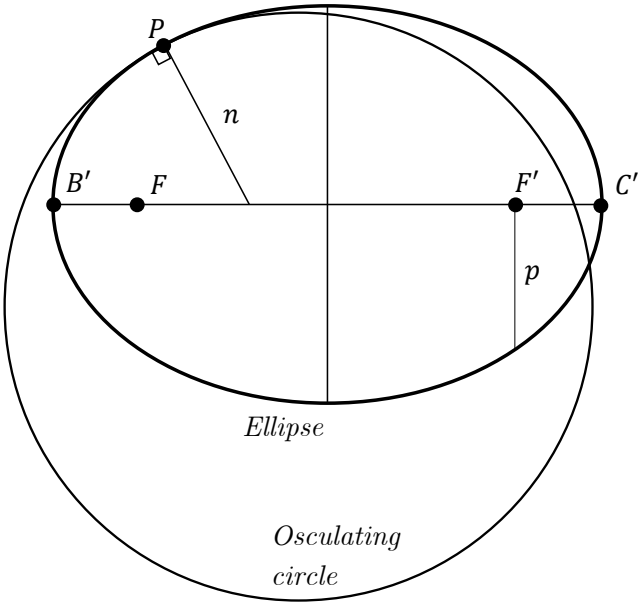

Figure 3: Osculating circle, freely adapted from [30].

Remark. The star streak is always close to the vertex point B'. By definition, the streak is symmetric with respect to the line joining B' and the FOV center.

Theorem 2. *With reference to Fig. 3, let P be a point on the conic, n the length of the normal from P to the axis and p half the length of the latus rectum (the latus rectum is the line segment through a focus perpendicular to the axis.) Then the radius of curvature at P, i.e. the radius of the osculating circle, is n^3/p^2 and the curvature at P is p^2/n^3.*

Proof. The proof can be found in [30]. ■

Remark. As a special case, when $P = B'$, the normal coincides with the major axis and n is not defined. However, $\lim_{P \to B'} n = p$, and the radius of curvature there is p (see [30]).

Theorem 3. *Given the eccentricity e of the conic, and the semi-aperture angle α of the cone generating the conic, then the angle β between $\hat{\boldsymbol{x}}_{\mathcal{S}}$ (i.e. the LOS)*

and $\hat{\boldsymbol{\omega}}$ (i.e. the axis of the cone) is given as

$$\beta = \sin^{-1}(e\cos\alpha)\,. \tag{3}$$

Moreover, calling with I the point of intersection between the axis of the cone and the focal plane, and defined A' as the FOV center (as in Fig. 2), the length of the segment $\overline{A'I}$ is given as

$$A'I = f\tan\beta. \tag{4}$$

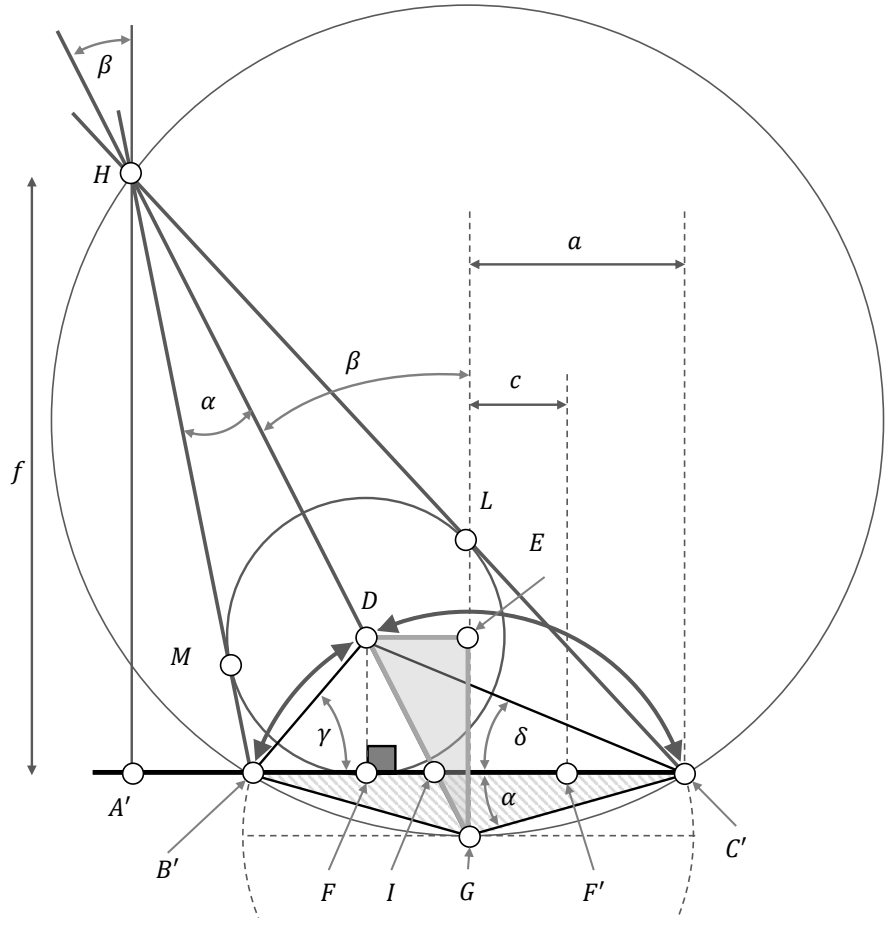

Figure 4: Drawing for the proof of Theorem 3.

Proof. The proof of this theorem is limited to the case of the ellipse, and is adapted from an on-line discussion [31] where some useful results were proved. For the proof, let Fig. 4 be considered. The figure lies entirely in the plane containing the major axis a of the ellipse (denoted here as the segment $B'C'$) and the LOS of the detector, where the segment $A'H$ is identified.

First, let the isosceles triangle $\triangle B'C'G$ be defined with base $\overline{B'C'}$ and base angle α. Construct a circle about G with radius $\overline{B'G}$. Let D be the intersection of this circle with the line through the focus F perpendicular to the major axis $\overline{B'C'}$, choosing the intersection nearer to F. Then, construct the circle around D with radius $\overline{DF}$. Construct the segments $\overline{C'L}$ and $\overline{B'M}$ tangent to that same circle at L and M, respectively. Let H bet the intersection of the extensions of the segments $\overline{C'L}$ and $\overline{B'M}$. Then H is the apex of the suitable cone and HD is the axis. To see this, observe that $\angle B'GC' = \pi - 2\alpha$. The same angle can be seen as the summation of the angles $\angle C'GD$ and $\angle B'GD$. Since the angle subtended by an arc at the centre is twice the angle subtended at the circumference, $\angle C'GD = 2\gamma$ and $\angle B'GD = 2\delta$. Accordingly, $\angle B'GC' = 2\gamma + 2\delta$. Therefore $2\alpha + 2\gamma + 2\delta = \pi$, and since two angles of the triangle $\triangle B'C'H$ are 2γ and 2δ, the third angle is 2α.

To prove Eq. (3), consider the right triangle $\triangle DEG$. The segment DE is equal to the distance to the focus $c = 0.5FF'$. The segments $\overline{DG}$ and $\overline{B'G}$ are congruent since they both are radii of the circumference centered in G. Moreover, $B'G = a/\cos\alpha$. Finally, the segments DE and DG are related as

$$DE = DG\sin\beta \Leftrightarrow c = \frac{a}{\cos\alpha}\sin\beta \tag{5}$$

Since $e = c/a$, Eq. (3) is proved by simply inverting Eq. (5). Finally, Eq. (4) is easily proved by looking at the right triangle $\triangle GHI$. ■

Remark. In three dimensions, the sphere with radius DF centered at D is a Dandelin sphere [32] for the intersection of the detector plane and the cone with apex H, axis HD, and semi-aperture angle α.

Unfortunately, all the properties described so far have no direct application

for the angular velocity determination since the features of the conics (eccentricity e and angle α) cannot be easily determined from the star streaks. Indeed, streaks are usually too short to allow one to exactly determine the conic parameters and, subsequently, the angular velocity. Accordingly, based on the properties described so far, a numerical approach, named chord method, is proposed and described in the following section.

3. Angular velocity determination

The determination of the angular velocity by means of images from a star sensor requires any algorithm to have two successive positions of the stars within the FOV. For instance, in [10], the position of the stars in two successive images was required to evaluate first-order finite differences which were then used to evaluate the angular velocity by means of the least square principle. This method is based on an analytical formulation which differs quite a bit from the proposed algorithm, which is based on geometrical investigations.

The identification of the angular velocity has been divided into three steps, each one describing a specific characteristic of the result. As it will be clear in the following sections, these scheme allows one to divide into successive steps the determination of the angular velocity basing on all the information provided by the couple of images. The three steps are briefly summarized below:

1. *Direction determination*: In the frame of this paper, the term "direction" refers to the line in $\mathcal{S}$ where the angular velocity lies, as reported in Fig. 5a. The direction is denoted as $\hat{\boldsymbol{\omega}}$ and, from the numerical point of view, it is associated to a unit vector with positive component along $\hat{\boldsymbol{x}}_{\mathcal{S}}$ (apart from singular cases where this component is null).
2. *Sign determination*: With the sign information the precise orientation of the angular velocity is evaluated. Referring to Fig. 5b, the angular velocity vector may lie in the identified direction in two different ways. The sign properly identifies the right orientation of the vector in the given direction as it is associated to a binary variable s which can assume values

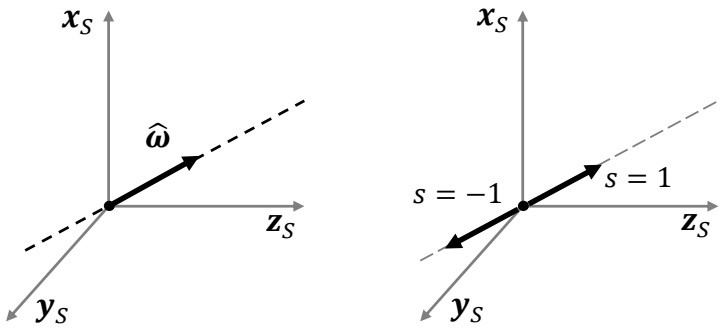

(a) (b)

Figure 5: Direction (a) and sign (b) of the angular velocity.

1 (when the angular velocity points in the direction of $\hat{\boldsymbol{x}}_{\mathcal{S}}$) and -1 (when the angular velocity points in the direction of $-\hat{\boldsymbol{x}}_{\mathcal{S}}$).

3. *Rate determination*: The magnitude is a positive number, ω, related to the length of the streak. This quantity is evaluated as a function of the velocity of the stars measured in the focal plane from two successive images.

The evaluation of the angular velocity is given using the three aforementioned contributions, i.e. direction $\hat{\boldsymbol{\omega}}$, sign s, and magnitude ω, and is finally given as

$$\omega = s\omega\,\hat{\boldsymbol{\omega}}. \tag{6}$$

The angular velocity error provided by the chord method estimation is then simply given as

$$\delta\boldsymbol{\omega} = \boldsymbol{\omega} - \boldsymbol{\omega}^{(ref)}, \tag{7}$$

where $\boldsymbol{\omega}^{(ref)}$ is the reference true angular velocity.

3.1. Direction determination with the chord method

Even though the geometrical relationships reported in the previous sections cannot be immediately used for the exact determination of the angular velocity vector, they can be used to design a method for the approximated estimation of the angular velocity direction.

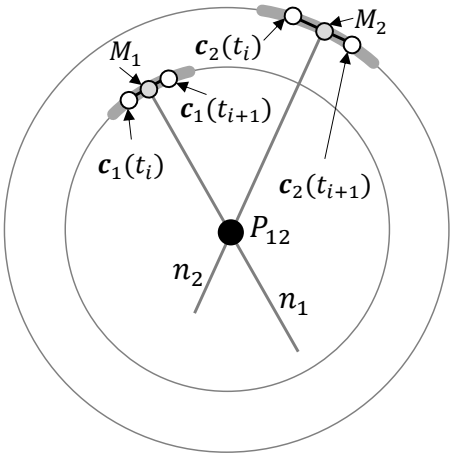

Figure 6: Circular case representation in the focal plane and application of the chord method.

3.1.1. Circular case

The most simple case is represented by the case $\boldsymbol{\omega} = [\omega_x,\ 0,\ 0]^{\mathsf{T}}$. Indeed, if $\hat{\boldsymbol{\omega}}$ is aligned with the LOS, the stars move along circles as represented in Fig. 6. In this case, the osculating circle coincides with the star trajectory in the focal plane and the length of the normal is equal to p which is indeed the distance between the star and the rotation center I.

Following the example in the figure, let two stars be detected in two successive images (the method exploited to merge stars in successive images is explained in Sec. 4.4). The centroids of the first and the second images can be easily evaluated (see Sec. 4 for technical details) and the equation of the jth chord passing through the jth couple of centroids is

$$a_{C,j}y + b_{C,j}z + c_{C,j} = 0. \tag{8}$$

The coefficients $a_{C,j}$, $b_{C,j}$, and $c_{C,j}$ are given by

$$\begin{aligned} a_{C,j} &= c_{j,z}(t_{i+1}) - c_{j,z}(t_i), \\ b_{C,j} &= c_{j,y}(t_i) - c_{j,y}(t_{i+1}), \\ c_{C,j} &= c_{j,y}(t_{i+1})c_{j,z}(t_i) - c_{j,y}(t_i)c_{j,z}(t_{i+1}). \end{aligned} \tag{9}$$

The coefficients of the normal to the chords passing through the midpoint M can be directly evaluated from the previous equations. Indeed, the jth normal is expressed as

$$a_{N,j}y + b_{N,j}z + c_{N,j} = 0 \tag{10}$$

and the coefficients are given as

$$\begin{aligned} a_{N,j} &= b_{C,j}, \\ b_{N,j} &= -a_{C,j}, \\ c_{N,j} &= -a_{C,j}M_{j,y} - b_{C,j}M_{j,z}. \end{aligned} \tag{11}$$

Considering the normal lines depicted in Fig. 6, the intersection point (x_{12}, y_{12}) is evaluated as solution of the following system of linear equations

$$\begin{cases} a_{N,1}x_{12} + b_{N,1}y_{12} + c_{N,1} = 0 \\ a_{N,2}x_{12} + b_{N,2}y_{12} + c_{N,2} = 0 \end{cases} \tag{12}$$

and is given by

$$\begin{aligned} x_{12} &= \frac{b_{N,1}c_{N,2} - b_{N,2}c_{N,1}}{a_{N,1}b_{N,2} - a_{N,2}b_{N,1}}, \\ y_{12} &= \frac{a_{N,2}c_{N,1} - a_{N,1}c_{N,2}}{a_{N,1}b_{N,2} - a_{N,2}b_{N,1}}. \end{aligned} \tag{13}$$

Given N_s stars in the FOV, the number of intersections N_I that can be evaluated is equal to

$$N_I = \frac{N_s!}{2(N_s - 2)!} \tag{14}$$

and is reported in Table 1 as a function of N_s.

The approximate position of I, denoted as $\tilde{I}$, can be found as the arithmetic average between the N_I intersections, i.e.

$$\tilde{I} = \frac{\sum_{i=1}^{N_s-1}\sum_{j=i+1}^{N_s}[x_{ij}, y_{ij}]^\mathsf{T}}{N_I} \tag{15}$$

The previous averaging operation can require a preliminary refinement of the results in order to avoid considering wrong intersections. In this work, the inter-decile method has been used.

Table 1: Number of measurements using the Chord Method.

Number of stars, N_s	Number of intersections, N_I
2	1
3	3
4	6
5	10
6	15
7	21
8	28
9	36
10	45

The performances of the proposed technique can be evaluated in an ideal scenario without noises, creating some example conics where the normal can be defined to calculate the intersection point.

A simplified example of the chord method is shown in Fig. 7, where 10 chords from the same conics defined by an angle α equal to 7 degree. As can be seen, the normal lines point to the rotation axis projection I. The geometrical features reported in the result section, especially in Table 4, are considered.

Another example is shown in Fig. 8, where $\beta = 0$ deg but 10 different values of α have been chosen. The normals have been taken from random points. As can be seen from Fig. 8b, the ideal intersection would be at the point $[0,\, 0]^{\mathsf{T}}$ and all the intersections are affected by very small errors due to numerical approximations.

Once the point $\tilde{I}$ is found, the angular velocity direction $\hat{\boldsymbol{\omega}}$ is evaluate by means of Eq. (1). In this simplified analysis no sign evaluation is needed, and the direction error is

$$\delta_{dir} = \cos^{-1}(\hat{\boldsymbol{\omega}} \cdot \hat{\boldsymbol{\omega}}_{true}). \tag{16}$$

The value of the direction error for the circular case is below the machine accu-

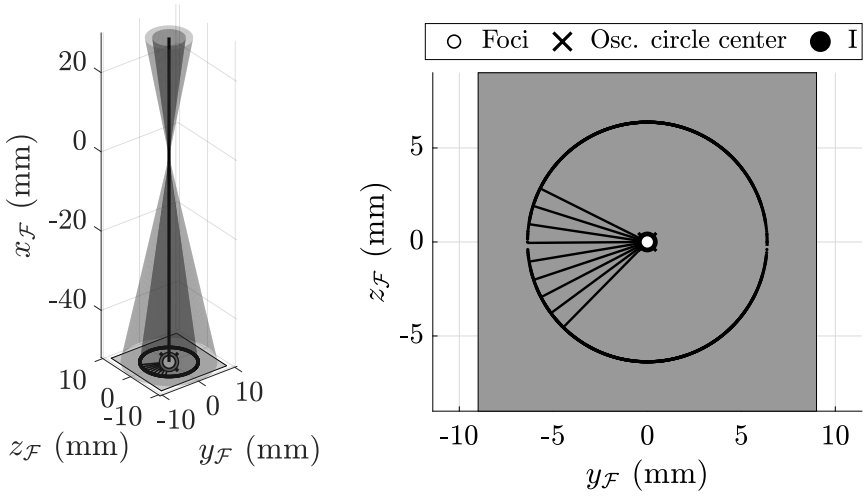

(a) (b)

Figure 7: 3D representation of the geometry with $\beta = 0$ deg and $\alpha = 7$ deg (a) and 2D projection on the $(y_{\mathcal{F}}, z_{\mathcal{F}})$ plane.

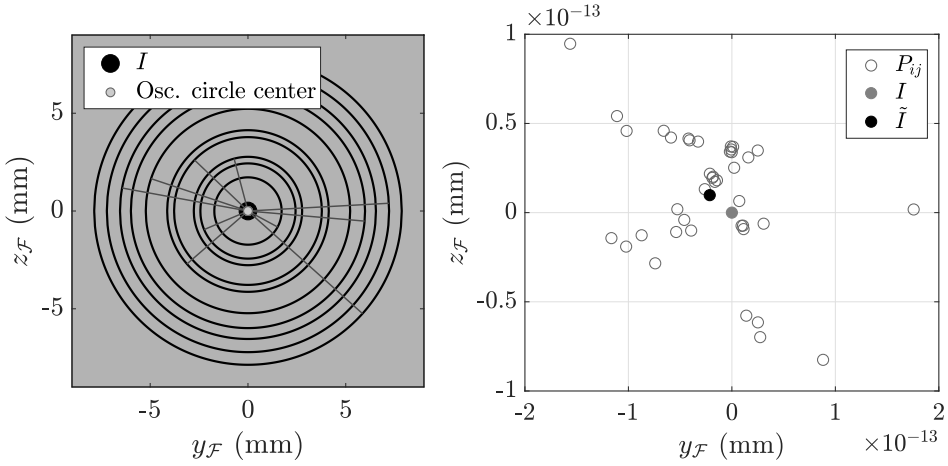

(a) (b)

Figure 8: Geometry of the problem (a) and chord method result (b) when $\beta = 0$ deg.

racy for a double-precision estimation, and it is reported in Table 2 along with the results for non-circular cases.

3.1.2. Generic case

When the conic is not a circle, the intersection between two normals is not directed toward the rotation axis projection point I. A preliminary and pretty qualitative analysis concerning sensors with small FOV, e.g. lower or equal to 20 degree, is the following. When conics are detected with small values of α, then the radius of the osculating circle does not change too much from p moving away from the vertex. On the contrary, when α increases, the portion of conic which is visible in the focal plane is close to the vertex (one can see this by looking at Fig. 4). Also in this case, the radius of the osculating circle does not differ too much from p since the osculating circle is evaluated close to the vertex. This observation justify the application of the chord method in non-circular cases.

Another property is related to the position of the osculating circle center as a function of the angles α and β. Indeed, when $\alpha < \beta$ then the radius of the osculating circle at the vertex of the conic (which is equal to p) is smaller than the distance of I from the FOV center. On the contrary, when $\alpha > \beta$, the radius of the osculating circle is greater than the distance of I from the FOV center. An example of the former case is reported in Fig. 9 for $\beta = 67.5$ deg and $\alpha = 60$ deg, whereas an example of the latter case si shown in Fig. 10 for $\beta = 67.5$ deg and $\alpha = 75$ deg,

When $\alpha = \beta$ the following theorem holds.

Theorem 4. *Let the angles α and β in Fig. 4 be congruent. Then, $\overline{B'I} \cong \overline{A'I}$ and $B'I$ and $A'I$ are given by Eq.* (4)*. Moreover, $B'I = A'I = p$.*

Proof. This proof is limited to the case of the ellipse. In this case, the focal length f can be expressed as a function of the semi-major axis a and the semi-aperture angle of the cone α. Indeed, referring to Fig. 4, when $\alpha = \beta$ then $A' \equiv B'$ and the focal length can be expressed as

$$f = 2a\cot(2\alpha). \tag{17}$$

Using Eq. (4) with $\alpha = \beta$, $A'I$ is evaluated as

$$A'I = f\tan\alpha$$

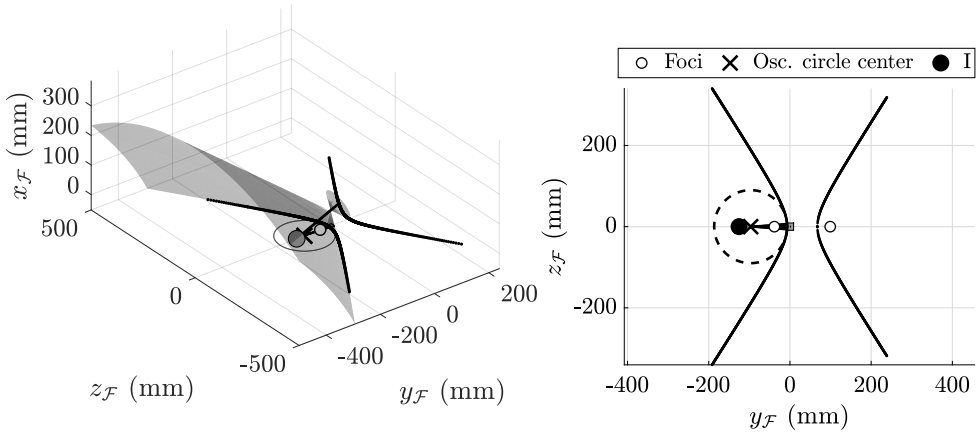

(a) (b)

Figure 9: 3D representation of the geometry with $\beta = 67.5$ deg and $\alpha = 60$ deg (a) and 2D projection on the $(y_\mathcal{F}, z_\mathcal{F})$ plane.

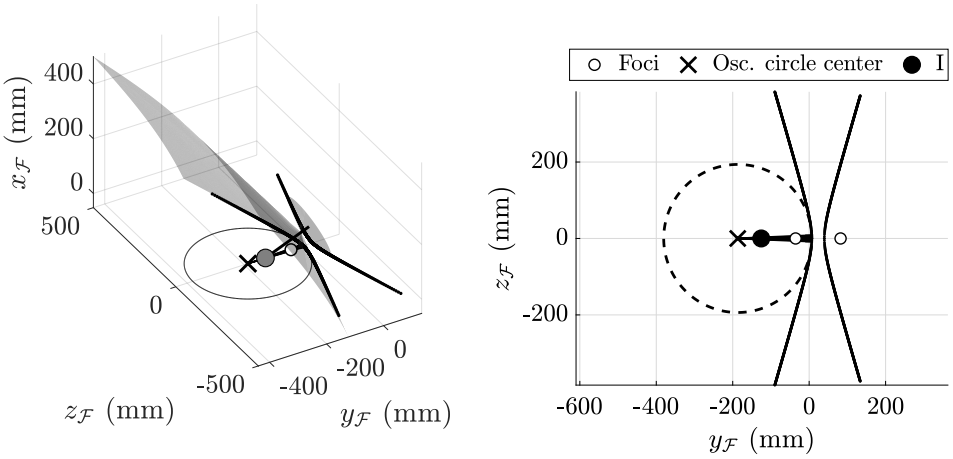

(a) (b)

Figure 10: 3D representation of the geometry with $\beta = 67.5$ deg and $\alpha = 75$ deg (a) and 2D projection on the $(y_\mathcal{F}, z_\mathcal{F})$ plane.

$$
\begin{aligned}
&= 2a \cot(2\alpha) \tan\alpha \\
&= 2a \frac{\cos(2\alpha)}{\sin(2\alpha)} \frac{\sin\alpha}{\cos\alpha} \\
&= 2a \frac{\cos^2\alpha - \sin^2\alpha}{2\sin\alpha\cos\alpha} \frac{\sin\alpha}{\cos\alpha}
\end{aligned}
\tag{18}
$$

$$= a\left(1 - \tan^2\alpha\right)$$

However, since $\alpha \cong \beta$, e can be expressed from Eq. (3) as

$$e = \tan\alpha. \tag{19}$$

It is a known fact that p is related to a and e as

$$p = a\left(1 - e^2\right). \tag{20}$$

Hence, using the previous result, p is given by

$$p = a\left(1 - \tan^2\alpha\right), \tag{21}$$

which coincides with the value of $A'I$. ■

Example of the direction determination with different values of β are shown from Fig. 11 to Fig. 14. On the left of each figure, the conics are shown with black lines, whereas the osculating circles are shown with dashed grey lines along with their centers. It can be seen how the osculating circles centers are placed both on the left and the right of the rotation center. The normal lines from random points of the conics are reported as well, whereas their intersection are shown on the right of every figure. Even though it may seen that the error on $\tilde{I}$ becomes bigger and bigger when β grows toward 90 degree, the angle errors are reported in Table 2.

In Table 2, the estimation $\tilde{I}_w$ is also reported. This is a weighted estimation of I based on the consideration that, generally, better solutions are found when the streaks are close to the FOV center (where it happens that $\alpha = \beta$). Accordingly, the weights w_{ij} can be introduced by defining

$$w_{ij} = \left(\frac{||\boldsymbol{M}_i|| + ||\boldsymbol{M}_j|| + \epsilon}{2}\right)^{-1}, \tag{22}$$

where $\epsilon = 1e - 16$ is introduced to avoid numerical singularities and $\boldsymbol{M}$ was defined in Fig. 6. From the definition, w_{ij} is quite low for streaks near the border and big for streaks close to the FOV center. Consequently, a weighted

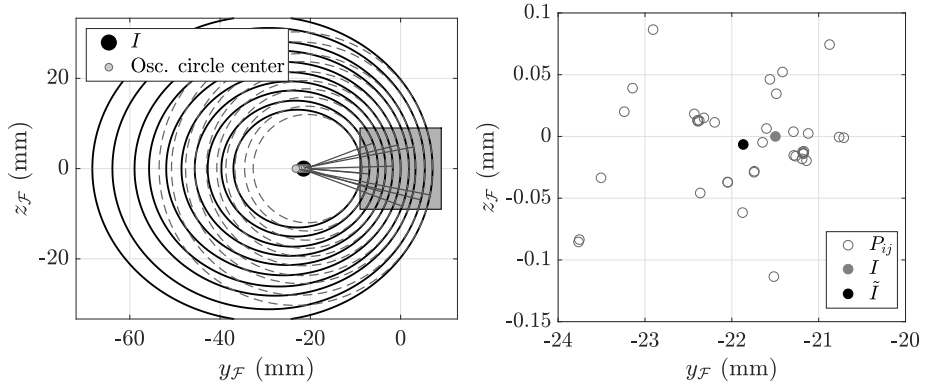

(a) (b)

Figure 11: Geometry of the problem (a) and chord method result (b) when $\beta = 22.5$ deg.

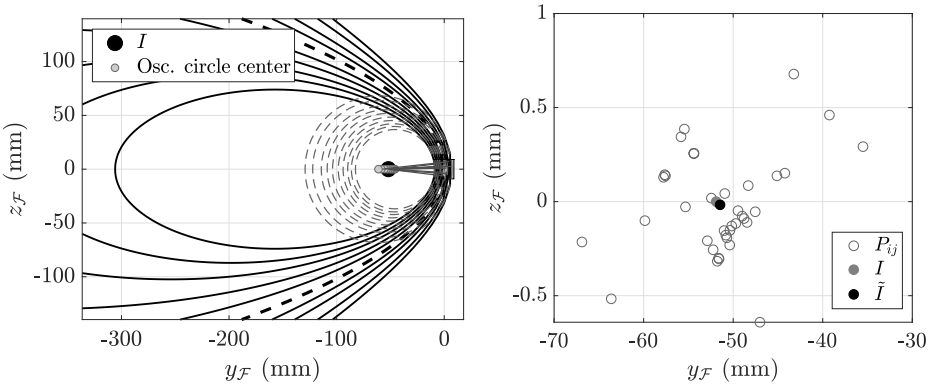

(a) (b)

Figure 12: Geometry of the problem (a) and chord method result (b) when $\beta = 45$ deg. The dotted line represents the parabola.

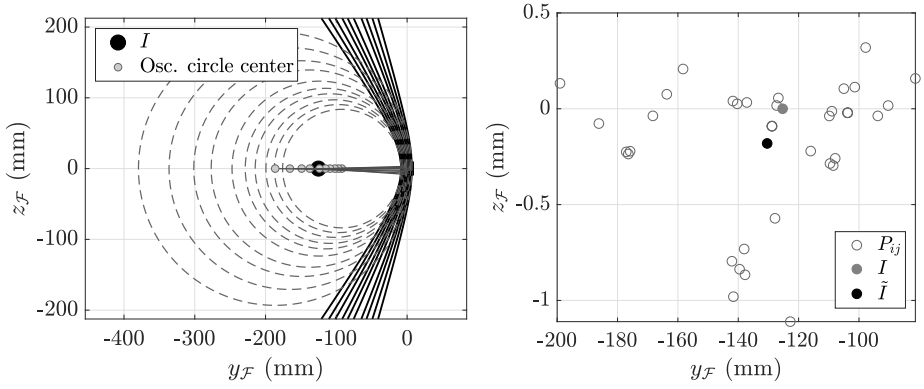

(a) (b)

Figure 13: Geometry of the problem (a) and chord method result (b) when $\beta = 67.5$ deg.

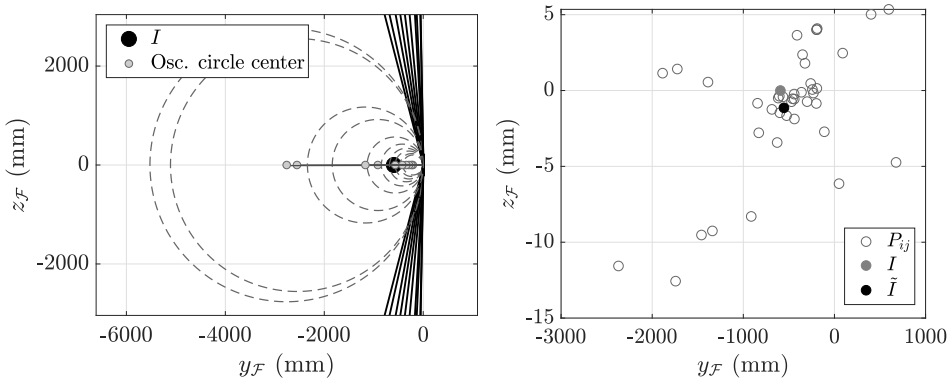

Figure 14: Geometry of the problem (a) and chord method result (b) when $\beta = 85$ deg.

Table 2: Direction error for the simplified model. The number $2.220 \cdot 10^{-16}$ is the machine accuracy of the double-precision result estimation.

β (deg)	δ_{dir} with $\tilde{I}$ (deg)	δ_{dir} with $\tilde{I}_w$ (deg)
0	$< 2.220 \cdot 10^{-16}$	$< 2.220 \cdot 10^{-16}$
22.5	0.307	0.261
45	0.241	0.308
67.5	0.484	0.561
85	0.368	0.083

average can be introduced to evaluate $\tilde{I}$ as

$$\tilde{I}_w = \frac{\sum_{i=1}^{N_s-1} \sum_{j=i+1}^{N_s} w_{ij} \left[x_{ij}, y_{ij}\right]^{\mathsf{T}}}{\sum_{i=1}^{N_s-1} \sum_{j=i+1}^{N_s} w_{ij}}. \tag{23}$$

However, looking at the results shown in Table 2, no clear evidence of performance improvement using $\tilde{I}$ is denoted, even though Monte Carlo analysis (which is beyond the scope of this work) is needed to properly validate this conclusion.

3.2. Sign determination via in-plane direction determination

As stated at the beginning of this section, any angular velocity determination method needs two successive images. For the algorithm proposed in this paper, two successive images are required to evaluate the direction of the stars related to their motion in the focal plane. To this aim, the centroid velocity evaluated from consecutive clusters is given as a first order finite difference, i.e.

$$\boldsymbol{v} = \frac{\Delta \boldsymbol{c}}{\Delta t} = \frac{\boldsymbol{c}(t_{i+1}) - \boldsymbol{c}(t_i)}{t_{i+1} - t_i}. \tag{24}$$

Using the centroids coordinates and the definition $T_{exp} = t_{i+1} - t_i$, the average cluster velocity is given as

$$v_y = \frac{c_y(t_{i+1}) - c_y(t_i)}{T_{exp}}, \quad v_z = \frac{c_z(t_{i+1}) - c_z(t_i)}{T_{exp}}. \tag{25}$$

Once v_y and v_z are evaluated, the sign value can be evaluated in a straightforward manner. Indeed, the motion of the stars around $\hat{\boldsymbol{\omega}}$ must happen in order to be consistent with v_y and v_z. Accordingly, $s = 1$ when the direction is consistent with v_y and v_z and $s = -1$ in the opposite case.

It is noteworthy that Eq. (25) must consider the distortion effects related to the read-out mode of the detector. Indeed, when a rolling shutter detector is used, the formula must take into account that the stars are not detected in the same time intervals and that these time intervals have different duration. The interested reader can refer to [27] for further information.

3.3. Rate determination from the streaks length

In the most general case, the star moves in a generic direction due to the angular velocity $\boldsymbol{\omega}^{(\mathcal{S})} = [\omega_x^{(\mathcal{S})},\ \omega_y^{(\mathcal{S})},\ \omega_z^{(\mathcal{S})}]^{\mathsf{T}}$. It is noteworthy that the component $\omega_x^{(\mathcal{S})}$ is responsible for the curvature of the streaks. Remembering the definition of the vector $\tilde{\boldsymbol{u}}$ provided in Eq. (2), and with reference to Fig. 1, the motion is represented by a rotation of the star vector in $\mathcal{S}$,

$$\boldsymbol{v} = \boldsymbol{\omega} \times \tilde{\boldsymbol{u}} = \begin{bmatrix} 0 & -\omega_z & \omega_y \\ \omega_z & 0 & -\omega_x \\ -\omega_y & \omega_x & 0 \end{bmatrix} \begin{bmatrix} x \\ y \\ z \end{bmatrix}, \tag{26}$$

which can be expressed in components as

$$\begin{aligned} v_x &= -\omega_z y + \omega_y z \\ v_y &= +\omega_z x - \omega_x z \\ v_z &= -\omega_y x + \omega_x y \end{aligned} \tag{27}$$

Note that the measurements that can be provided by the star sensor are only v_y and v_z, i.e. only the projection of the velocity in the focal plane. Let decompose the angular velocity vector in accordance to Eq. (6), i.e.

$$\boldsymbol{\omega} = s\omega \left[\hat{\omega}_x^{(\mathcal{S})},\ \ \hat{\omega}_y^{(\mathcal{S})},\ \hat{\omega}_z^{(\mathcal{S})}\right]^{\mathsf{T}}. \tag{28}$$

Eq. (27) can be rewritten as

$$\begin{aligned} v_x &= s\omega\left(-\hat{\omega}_z y + \hat{\omega}_y z\right) \\ v_y &= s\omega\left(+\hat{\omega}_z x - \hat{\omega}_x z\right) \\ v_z &= s\omega\left(-\hat{\omega}_y x + \hat{\omega}_x y\right) \end{aligned} \tag{29}$$

Introducing the norm of the velocity in the image plane, v^*, evaluated as

$$v^* = \sqrt{v_y^2 + v_z^2}, \tag{30}$$

and given that $s^2 = 1$, the angular velocity magnitude can be evaluated from Eq. (29) as

$$\omega = \frac{v^*}{\sqrt{\left(+\hat{\omega}_z x - \hat{\omega}_x z\right)^2 + \left(-\hat{\omega}_y x + \hat{\omega}_x y\right)^2}}, \tag{31}$$

Eq. (31) can be applied for the evaluation of the rate by choosing $[x,\, y,\, z]^{\mathsf{T}}$ as the midpoint of the streak. The relative rate error is evaluated as

$$\delta_{rate} = \omega - \omega_{true}. \tag{32}$$

Considering a constant angular velocity during the exposure time, this model is correct when $\omega_x = 0$. On the other hand, when $\omega_x \neq 0$, an estimation error is committed since $v*$ is evaluated basing on the measurable quantities v_y and v_z which are calculated considering a linear motion (with constant speed) instead

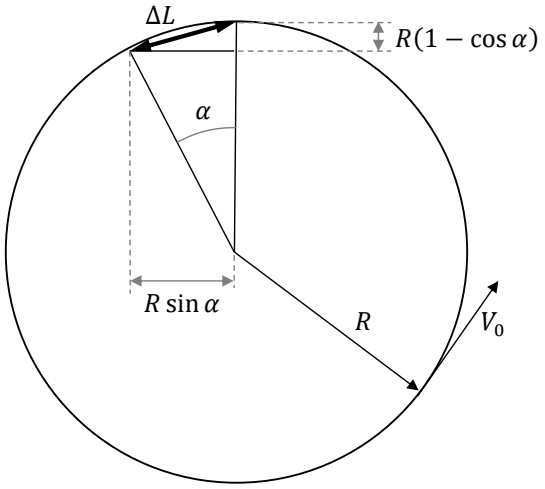

Figure 15: Linear approximation of arcs on a circle.

of a circular motion (with constant speed). When $\boldsymbol{\omega}^{(\mathcal{S})} = [\omega_x^{(\mathcal{S})},\ 0,\ 0]^\mathsf{T}$, the tangential velocity v_0 is related to the angular velocity as

$$v_0 = \omega_x R, \tag{33}$$

where R is the distance of the star centroid from the FOV center and

$$\omega_x = \alpha / T. \tag{34}$$

The velocities v_y and v_z are evaluated using the linear approximation of the circle, ΔL, depicted in Fig. 15 and given by

$$\begin{aligned} \Delta L^2 &= R^2 \left(1 - \cos\alpha\right)^2 + R^2 \sin^2\alpha \\ &= R^2 \left(\sin^2\alpha + \cos^2\alpha - 2\cos\alpha + 1\right) \\ &= 2R^2 \left(1 - \cos\alpha\right). \end{aligned} \tag{35}$$

Consequently, the ratio between ΔL and T is given by

$$\frac{\Delta L}{T} = \frac{R}{T}\sqrt{2}\sqrt{1 - \cos\alpha} \tag{36}$$

It is noteworthy that the ratio between ΔL and T corresponds to v^*. Hence,

evaluating the time from Eq. (34), Eq. (36) can be cast as

$$v^* = v_0\sqrt{2}\frac{\sqrt{1-\cos\alpha}}{\alpha} = \epsilon v_0, \tag{37}$$

where ϵ is defined as an approximation scale factor. Anyway, considering a very high value for ω_x such as 20 deg/s and an exposure time $T = 0.2$ seconds, the value of ϵ is 0.9998, which makes it reasonable to use v^* for the evaluation of the angular velocity rate in any dynamic condition. Moreover, it can be seen that when $\alpha \to 0$ then $1 - \cos\alpha \to \alpha^2/2$, so that $\epsilon \to 1$ as expected, since in this singular case linear and circular motion tend to coincide.

4. Processing of the image

In the result section, the proposed algorithm is tested using the high fidelity simulator described in details in [25, 26, 27, 28, 33]. This simulator considers all the physical and geometrical characteristics of the star sensor, along with all the instrumental and environmental noises. To correctly deal with streaks in dynamic conditions, a specific processing of the image is required. Indeed, in dynamic conditions stars are detected as streaks, and dim stars are seen as broken streaks as their energy is spread over a big amount of pixel. The following preprocessing and processing operations are introduced to collect all the pixels belonging to the stars into properly defined clusters.

4.1. Preprocessing

The high-energy pixels belonging to the star signals must be distinguished from the low-energy pixels where only noise is recorded. Accordingly, an image preprocessing selects the pixels whose signal-to-noise ratio (SNR) is greater than a user-defined detection threshold and discards the other ones [34]. This preliminary operation is referred to as segmentation and it is usually performed using a run-length encoding algorithm [35].

The segmentation algorithm can be implemented using a static (global) or a dynamic (local) approach [36]. The SNR is evaluated considering the same

background noise for the static approach and a specific background noise for each pixel of the detector for the dynamic approach. A survey of different techniques is reported in [37]. In this work, a zigzag local thresholding using moving averages is used [38]. Hence, the only pixels that are considered for further investigations are those with values greater than the background level (evaluated with moving average) plus a threshold τ_{pre}. It is noteworthy that quantization errors can occur due to pixel discretization of the image.

The outputs of the preprocessing operation are the selected pixels' coordinates $\boldsymbol{p} = [p_y, p_z]^T$ and their energy $E(\boldsymbol{p})$, obtained subtracting the background level to the entire signal intensity of the pixel.

4.2. Primitive clustering

Once the pre-processed image is computed, an algorithm is needed to recognize all the neighboring pixels belonging to individual stars, and this operation is referred to as clustering. Accordingly, the set of pixels belonging to the ith star is referred to as ith cluster and denoted with $\mathscr{C}_i$. The generic pixel associated to the cluster $\mathscr{C}_i$ is denoted as $\boldsymbol{p}^{(\mathscr{C}_i)} = [p_y^{(\mathscr{C}_i)}, p_z^{(\mathscr{C}_i)}]^\mathsf{T}$. Usually, star sensors carry out a simple algorithm denoted here as primitive clustering. However, this typical function is not enough when dealing with fast objects, and the following

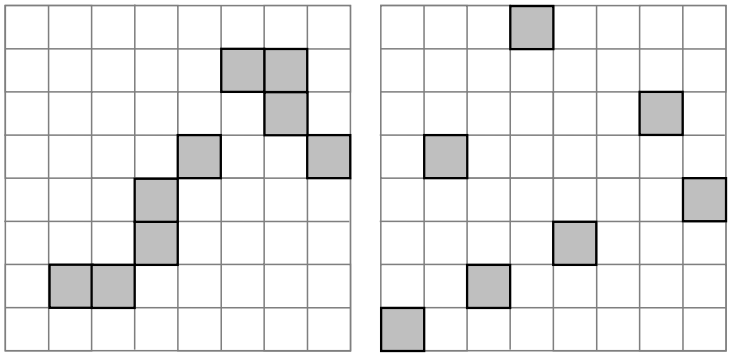

(a) *Primitive clusters* (b) *Noise*

Figure 16: Example of two primitive clusters (a) and example of discarded single pixels (b).

improved clustering has been introduced to cope with this issue.

The evaluation of the *primitive* clusters is concerned with finding the pixels which share at least one corner. The primitive clustering working principle is shown in Fig. 16a, where two examples of primitive clusters are represented. Single pixels shown in Fig. 16b are mostly related to noise or too faint stars or RSOs and they are automatically discarded and not considered for the following analyses.

4.3. Improved clustering

Under dynamic conditions, stars can generate broken streaks, i.e. the pixels belonging to the same star can distribute into several, small and distinct clusters. Hence, a suitable technique has been developed in order to relate to the same star the different primitive clusters of the broken streak. The technique must avoid wrong primitive clusters agglomeration coming from noise or wrong matching between different objects. Clusters $\mathscr{C}_i$ and $\mathscr{C}_j$ can be merged if they satisfy the conditions described in the following subsections.

4.3.1. Minimum distance filter

The distance between clusters $\mathscr{C}_i$ and $\mathscr{C}_j$ must be lower than a user-defined threshold ε_{dist}. It is noteworthy that the distance between clusters is referred to as δ_{min} and it is evaluated as minimum pixel-by-pixel distance using the uniform norm, according to what is shown in Fig. 17. The minimum distance condition is defined as

$$\delta_{min} \leq \varepsilon_{dist}. \tag{38}$$

Fig. 17 shows this condition for two clusters imposing $\varepsilon_{dist} = 3$. In Fig. 17a the satisfied condition is reported since $\delta_{min} = 2$, whereas in Fig. 17b the condition is not satisfied as $\delta_{min} = 4$. If the minimum distance conditions is satisfied, the clusters are considered for the following increasing length check.

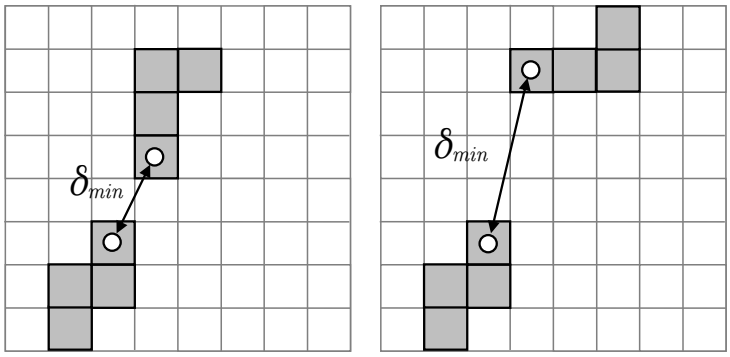

(a) *Condition satisfied* (b) *Condition not satisfied*

Figure 17: Minimum distance condition

4.3.2. Increasing length filter

Let $\boldsymbol{l}_i = [l_{y,i}, l_{z,i}]$ be the length vector of $\mathscr{C}_i$ collecting the horizontal and vertical projections of the cluster defined as

$$l_{y,i} = \max p_y^{(\mathscr{C}_i)} - \min p_y^{(\mathscr{C}_i)} + 1, \quad l_{z,i} = \max p_z^{(\mathscr{C}_i)} - \min p_z^{(\mathscr{C}_i)} + 1. \tag{39}$$

To merge $\mathscr{C}_i$ and $\mathscr{C}_j$, the resulting merged cluster $C_{ij} = \mathscr{C}_i \cup \mathscr{C}_j$ must satisfy three conditions related to $\boldsymbol{l}_i$, $\boldsymbol{l}_j$ and $\boldsymbol{l}_{ij}$.

The first condition relates to those merged clusters that increase both the horizontal and vertical projections and is described by the variable L_1 defined as

$$L_1 = \begin{cases} 1 & \text{if} \quad l_{y,ij} > \max\left(l_{y,i}, l_{y,j}\right) \text{ and} \\ & \qquad l_{z,ij} > \max\left(l_{z,i}, l_{z,j}\right) \\ 0 & \text{otherwise.} \end{cases} \tag{40}$$

This condition can describe the clusters which have intermediate inclinations between 0 and 90 degrees in the $\{\boldsymbol{y}_{\mathcal{F}}, \boldsymbol{z}_{\mathcal{F}}\}$ plane. However, when the clusters are quite horizontal or vertical, the flag L_1 can be misleading since one of the two projections can remain stationary instead of increase. Accordingly, two new complementary conditions are introduced and related to the flags L_2 and

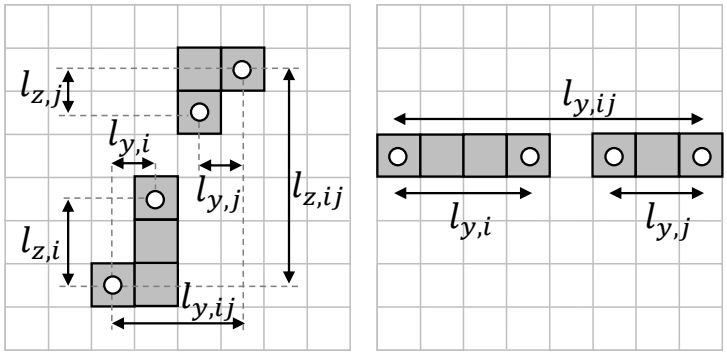

(a) $L_1 = 1$ (b) $L_2 = 1$

(c) $L_3 = 1$ (d) $L_1 = L_2 = L_3 = 0$

Figure 18: Increasing length condition

L_3 defined as

$$L_2 = \begin{cases} 1 & \text{if} \quad l_{y,ij} > \max\left(l_{y,i}, l_{y,j}\right) \text{ and } l_{y,ij} > l_{z,ij} \\ 0 & \text{otherwise,} \end{cases} \tag{41}$$

$$L_3 = \begin{cases} 1 & \text{if} \quad l_{z,ij} > \max\left(l_{z,i}, l_{z,j}\right) \text{ and } l_{z,ij} > l_{y,ij} \\ 0 & \text{otherwise.} \end{cases} \tag{42}$$

Fig. 18 reports a representation of the three conditions. In Fig. 18a the case with $L_1 = 1$ is shown and the projections of the merged cluster are greater than the ones of the primitive clusters. In Fig. 18b and Fig. 18c the horizontal and

vertical case are shown respectively. Note that in these cases $L_1 = 0$. Finally, in Fig. 18d none of the three checks is satisfied. To proceed with the density check, at least one of the three values L_1, L_2 and L_3 must be equal to 1.

4.3.3. Density filter

Clusters $\mathscr{C}_i$ and $\mathscr{C}_j$ can be merged if they satisfy some necessary conditions related to their densities. For the cluster $\mathscr{C}_i$, the density is defined as

$$d_i = \frac{N_i}{\lambda_i} \tag{43}$$

where N_i is the number of pixels belonging to the i^{th} cluster and

$$\lambda_i = \sqrt{(l_{y,i}\cos\alpha_i)^2 + (l_{z,i}\sin\alpha_i)^2}. \tag{44}$$

In Eq. (44) α_i denotes the angle given as

$$\alpha_i = \tan^{-1}\left(\frac{l_{z,i}-1}{l_{y,i}-1}\right). \tag{45}$$

The quantity λ_i represents a virtual length which works fine for the definition of the density without requiring a complicated computation. The density filter performs two separate checks. First, the relative difference between the two clusters' density must be lower than a user defined threshold $\varepsilon_{dens,rel}$. The relative density difference is defined as

$$\delta d = \frac{|d_i - d_j|}{d_{ij}} \tag{46}$$

where d_i and d_j are the densities of the single primitive clusters and d_{ij} is the density of the merged cluster. The filter output is described by the variable D_1 defined as

$$D_1 = \begin{cases} 1 & \text{if} \quad \delta d < \varepsilon_{dens,rel} \\ 0 & \text{otherwise.} \end{cases} \tag{47}$$

With reference to the example case reported in Fig. 19a the densities of primitive and merged clusters are

$$d_1 = 1, \quad d_2 = 1, \quad d_{12} \approx \frac{5}{5.63} \approx 0.8879,$$

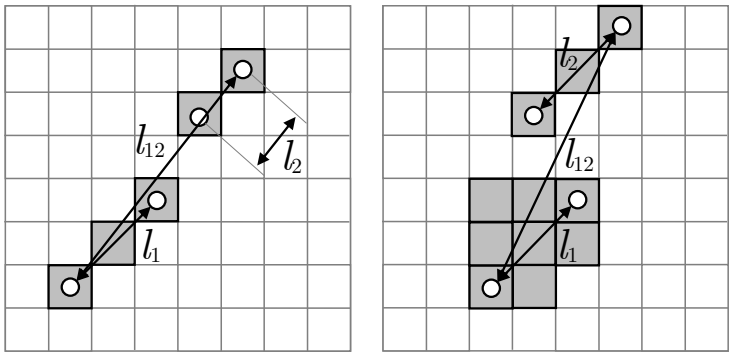

(a) $D_1 = 1$ (b) $D_1 = 0$

Figure 19: Similar density condition with $\varepsilon_{d,rel} = 0.5$

leading to $\delta d = 0$ and $D_1 = 1$, i.e. the first density check is satisfied. On the contrary, for the case in Fig. 19b, the densities are

$$d_1 = \frac{8}{3} \approx 2.6667, \quad d_2 = 1, \quad d_{12} = \frac{11}{\sqrt{65}} \approx 1.6893,$$

and $\delta d = 0.9866$. Considering $\varepsilon_{dens,rel} = 0.5$, $D_1 = 0$ for the case (b).

However, the previous check makes sense when applied to clusters with low density values which are likely to be broken into different pieces. To consider this point, a second density check is introduced with a new variable D_2 defined as

$$D_2 = \begin{cases} 1 & \text{if} \quad \max(d_i, d_j) < \varepsilon_{dens,abs} \\ 0 & \text{otherwise,} \end{cases} \tag{48}$$

where $\varepsilon_{dens,abs}$ is a user-defined threshold.

The density filter is successfully passed if $D_1 = D_2 = 1$.

4.3.4. Centroid computation

After the application of the previous filters, some primitive clusters have been merged and others are not. The clusters centroids of all the detected and processed clusters can now be computed. The centroid $\boldsymbol{c}_i = [c_{y,i}, c_{z,i}]^\mathsf{T}$ is the reference position of the i^{th} cluster $\mathscr{C}_i$ and it is computed using the pixels

coordinates $\boldsymbol{p} = [p_y, p_z]^\mathsf{T} \in \mathscr{C}_i$ throughout an energy-weighted average, i.e.

$$\boldsymbol{c}_i = \frac{1}{E_{\mathscr{C}_i}} \sum_{j|\boldsymbol{p}_j \in \mathscr{C}_i} E(\boldsymbol{p}_j) \cdot \boldsymbol{p}_j, \tag{49}$$

where $E(\boldsymbol{p}_j)$ is the signal intensity of the pixel $\boldsymbol{p}_j$ and

$$E_{\mathscr{C}_i} = \sum_{j|\boldsymbol{p}_j \in \mathscr{C}_i} E(\boldsymbol{p}_j) \tag{50}$$

is the total signal intensity of the i^{th} cluster.

4.4. Cluster fusion

The cluster fusion is the operation required to compare two successive images and merge those streaks or spots that are supposed to belong to the same star. The proposed algorithm is designed to work with successive images, i.e. it cannot be applied if a non-negligible time interval separates the first and the second image, and the required operations resemble the the ones described in Sec. 4.2 and Sec. 4.3 for the clustering.

Consider two successive images with $N_{c,1}$ and $N_{c,2}$ detected clusters, respectively. Let the cluster $\mathscr{C}_j(t_i)$ be considered in the first image associated to the time instant t_i, where $1 < j < N_{c,1}$. This cluster will be compared with the cluster $\mathscr{C}_k(t_{i+1})$ in the second image associated to the time instant t_{i+1}, where $1 < k < N_{c,2}$. The minimum distance filter is applied as described in Sec. 4.3.1. The density filter is applied considering only the D_1 parameter in Eq. (51). The same concept used for D_1 is used to compare the length of $\mathscr{C}_j(t_i)$ and $\mathscr{C}_k(t_{i+1})$, i.e.

$$L_{fus} = \begin{cases} 1 & \text{if} \quad \delta l < \varepsilon_{len,rel} \\ 0 & \text{otherwise} \end{cases} \tag{51}$$

where

$$\delta l = \frac{|l_j - l_k|}{l_{jk}} \tag{52}$$

and $\varepsilon_{len,rel}$ is a user-defined parameter. It is noteworthy that the output from the fusion does not contain not-merged clusters, i.e. clusters that do not appear in both the successive images. The output of the fusion represents the information required for the evaluation of the in-plane star velocity of Eq. (25).

5. Numerical results and analysis

The result section is dedicated to the analysis of the results provided by the chord method. Firstly, an analysis of the number of the stars depending on the angular rate is reported. Then, results with fixed angular velocities are discussed and, finally, results with a variable angular velocity profile are provided. The numerical values of the parameters required by the algorithm are reported in Table 3. The main characteristics of the adopted high fidelity image simulator are given in Table 4 and, finally, the noise sources taken into account are shown in Table 5 with their related properties. Note that 100 SEUs per image have been added to test the robustness of the proposed clustering and fusion algorithm. For all the reported simulations, the initial attitude is given by the quaternion

$$q_0^{\mathcal{C}\to ECI} = [-0.485,\ -0.134,\ 0.833,\ -0.231]^{\mathsf{T}} \tag{53}$$

which defines the mapping from the camera reference frame $\mathcal{C}$ to the Earth-centered inertial (ECI) reference frame. The errors of the angular velocity estimation are provided by Eq. (7), Eq. (16), and Eq. (32).

5.1. Number of detected stars

The first analysis is related to the number of detected stars as a function of the angular rate. The angular velocity direction is imposed as

$$\hat{\boldsymbol{\omega}}^{(ref)} = [0.2673,\ -0.5345,\ 0.8018]^{\mathsf{T}}, \tag{54}$$

Table 3: Parameters of the software.

Parameter	Ref.	Value
ε_{dist}	Sec. 4.3.1	3 pixel
$\varepsilon_{dens,rel}$	Sec. 4.3.3	0.5
$\varepsilon_{dens,abs}$	Sec. 4.3.3	1.75 pixel^{-1}
$\varepsilon_{len,rel}$	Sec. 4.4	0.5

Table 4: Main characteristics of the image simulator.

Sensor characteristic	Adopted value
Detector	1024 × 1024 Active Pixel Sensor (APS)
Field of View (FOV)	20 × 20 deg
Focal length f	52 mm
Exposure time T_{exp}	0.2 s
Pixel dimensions	18 × 18 µm
Simulated stars magnitude $\mathcal{M}_S$	$\mathcal{M}_S \leq 6.5$
On-board catalog	Hipparcos stars with $\mathcal{M}_C \leq 5.5$
G_0	7300000 e^-/s
τ_{pre}	500 e^-
d_f	2 pixel

Table 5: Main characteristics of noise sources.

Noise sources	Adopted model
Dark current	Normal distribution: 100 e^- mean and 5 e^- std [39].
Stray-light	Uniform value of 6000 e^- over the whole detector.
Shot noise	Poisson probability distribution proportional to the square root of the detected signal[40].
Read-out noise	Normal distribution: 0 mean and 50 e^- std [41].
SEUs	Uniform flux of 100 SEUs per image [33].

whereas the norm of the angular velocity is imposed equal to 1, 2, 3, 4, 5 deg/s. The simulation time is imposed equal to 100 seconds.

The number of stars detected by the simulator is shown in Fig. 20. It is noteworthy that increasing the angular rate the number of detected stars decreases. This is consistent with the fact that the stars spend less time over single pixels and the number of associated photoelectrons diminish as well as the signal to noise ratio. Accordingly, dim stars with magnitude around 4 and 5

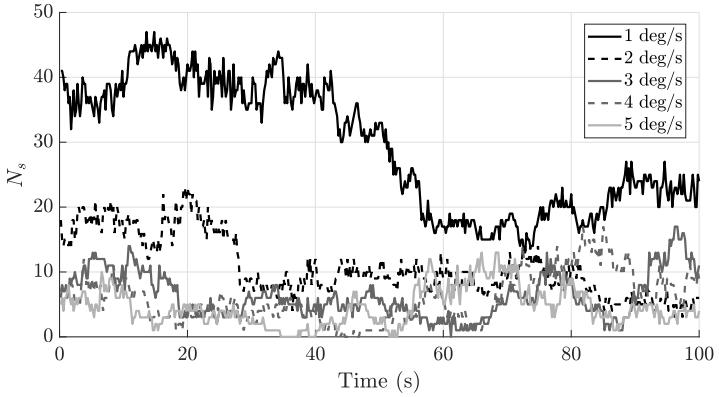

Figure 20: Number of detected stars in the FOV with rates from 1 to 5 deg/s.

that are detected when $||\boldsymbol{\omega}|| = 1$ deg/s are no more detected when $||\boldsymbol{\omega}||$ is around 4 or 5 deg/s. This fact is quite important considering that it strongly affects the precision of the chord method estimation. Indeed, when the number of detected stars is very low, the algorithm does not provide any measurement or gives very bad results. It is also important to note that the number of detected stars can change even with fixed rates. For instance, looking at the curve at 1 deg/s, the number of stars at the beginning is approximately 40 and it is almost twice the number of stars detected in the time interval between 60 and 80 seconds. This is due to the fact that stars in the sky are not uniformly distributed and varying the pointing the number and the magnitude of the stars continuosly change.

5.2. Results with fixed angular velocity

These results have been obtained with the angular velocity profiles discussed in the previous section and a simulation time equal to 100 seconds.. Direction and rate errors are reported in Fig. 21. Looking at the plots on the left of Fig. 21, it can be seen that when $||\boldsymbol{\omega}||$ is equal to 1 deg/s the direction errors are quite always very small apart from 4 peaks where the error is more than 10 degree. Increasing the angular velocity the number of peaks become greater and this is due to the fact that sometimes only few and dim streaks are available.

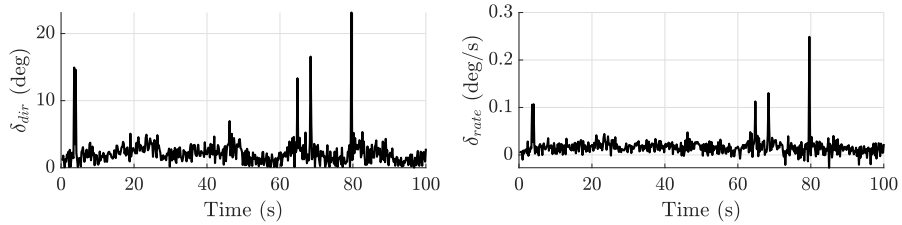

(a) 1 deg/s

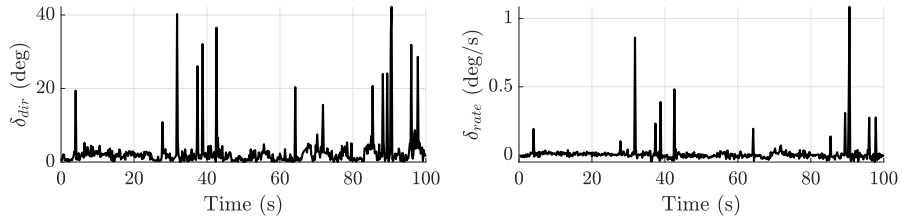

(b) 2 deg/s

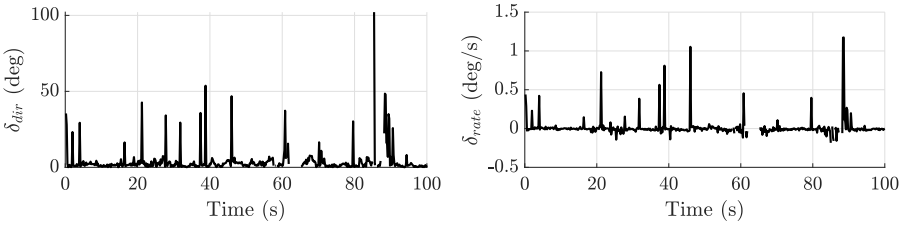

(c) 3 deg/s

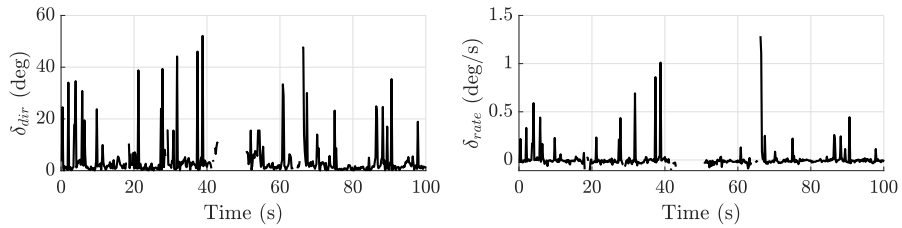

(d) 4 deg/s

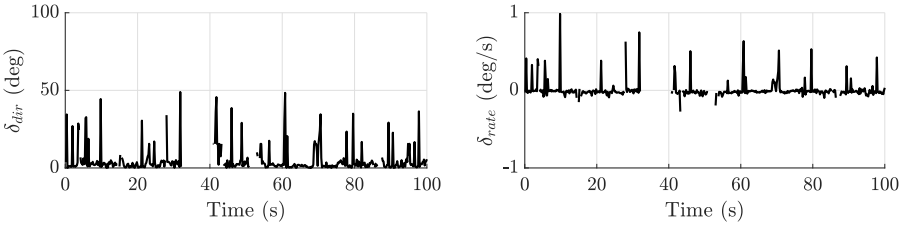

(e) 5 deg/s

Figure 21: Direction error (on the left) and rate error (on the right) of the chord method with rates from 1 to 5 deg/s and fixed direction.

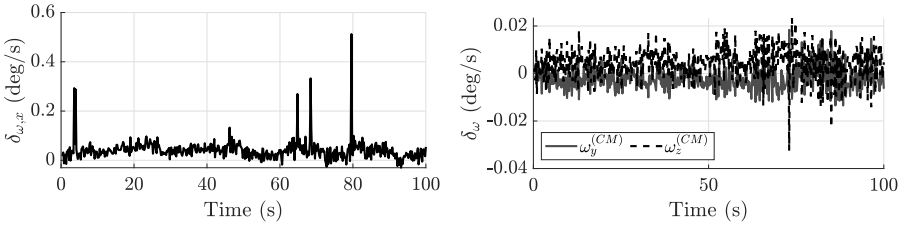

(a) 1 deg/s

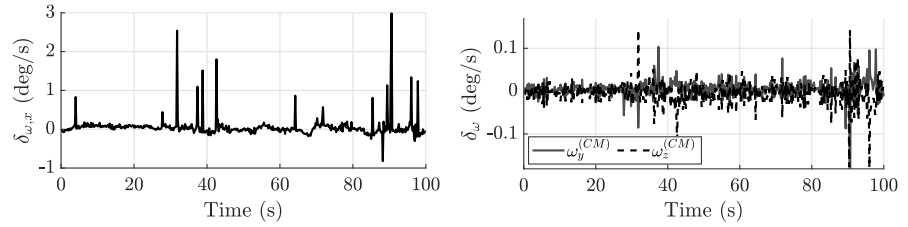

(b) 2 deg/s

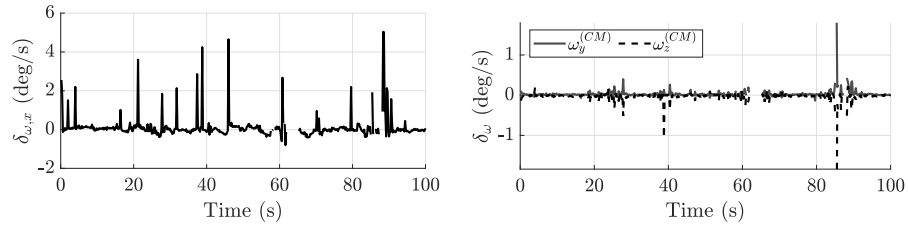

(c) 3 deg/s

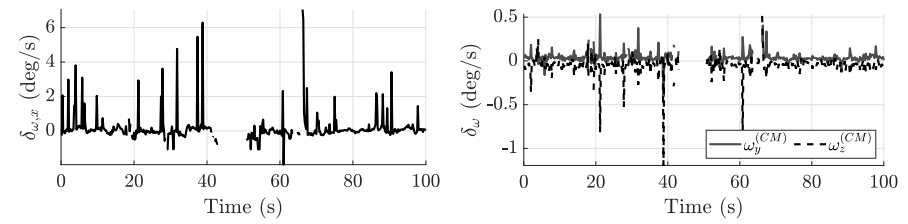

(d) 4 deg/s

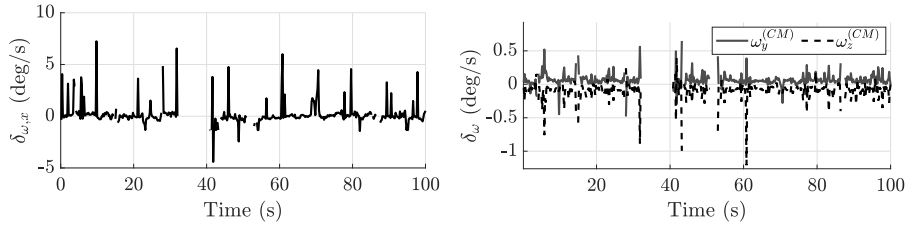

(e) 5 deg/s

Figure 22: Angular velocity errors along the x component (on the left) and the y, z components (on the right) of the chord method with rates from 1 to 5 deg/s and fixed direction.

Eventually, the magnitude of the peaks increases with bigger angular rates, but they are quite always below 90 degree. This is particularly important if one want to use these measurements to reduce the angular velocity of a spacecraft. Another interesting fact is that, starting from a rate equal to 3 deg/s, one can note some time intervals where no measurement is provided because the chord method wasn't able to run (less than 2 stars were available).

The rate determination behaves similarly to the direction error as far as peaks and no-measurment intervals is concerned. However, looking at the plots on the right of Fig. 21, it can be seen that maximum errors are always below 1 deg/s apart from very rare cases. It is noteworthy that such errors are obtained only when a very small number of stars are detected. When the number of stars is reasonable high, the relative norm errors are quite reduced.

The errors of the angular velocity estimates divided by components is shown in Fig. 22. Here one can appreciate that the bigger errors are obtained along the line of sight, i.e. along the x axis, where some error peaks around 5 deg/s are reported. On the contrary, errors along y and z are of the same order of magnitude and quite always below 0.5 deg/s. This is completely consistent with the star tracker performances in attitude determination mode, where roll errors are always bigger then yaw and pitch errors. Obviously, such errors can be drastically reduced and uniformed using a multi-head architecture for compensation of the errors along the line of sight.

5.3. Results with variable velocity

This test case deals with an angular velocity which is given by

$$\boldsymbol{\omega} = (5 - 4t/T)\,\frac{\boldsymbol{d}}{\|\boldsymbol{d}\|}\ \text{deg/s}, \tag{55}$$

where the norm is linearly decreasing from 5 to 1 deg/s and

$$\boldsymbol{d} = \left[0.8452\cos(0.01t),\ -0.5345,\ -0.4795\sin(0.005t)\right]^{\mathsf{T}}, \tag{56}$$

imposing a user-defined sinusoidal law to the direction. The simulation time interval T is equal to 1000 seconds. This can represent a generic situation where

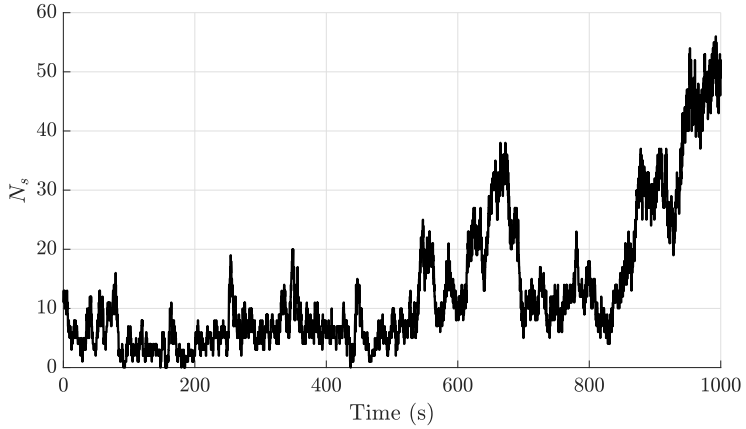

Figure 23: Number of detected stars in the FOV with variable velocity.

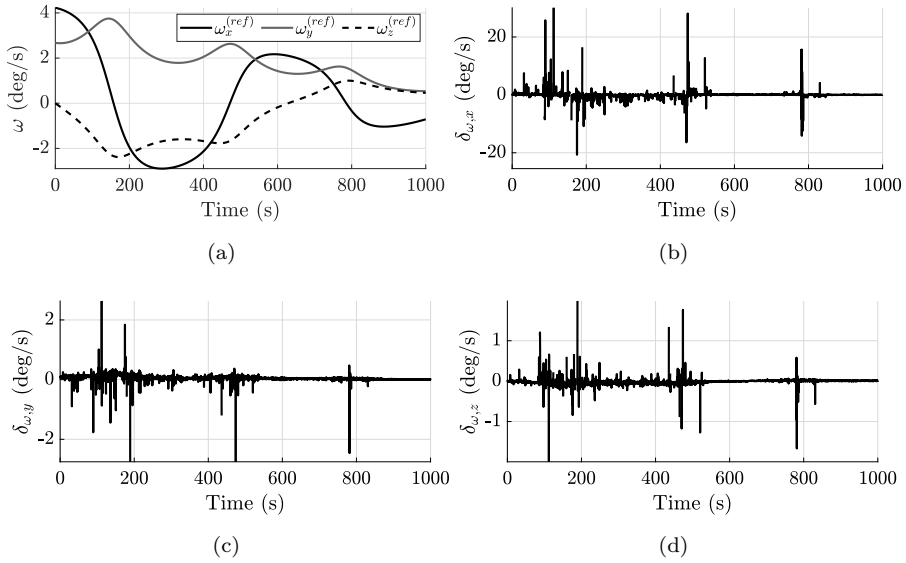

Figure 24: Simulated angular velocity profile (a) and chord method errors for x (b), y (c), and z (d) component.

a tumbling spacecraft is slowly controlled in order to reduce the initial angular rate. The imposed profile is depicted in Fig. 24a. The number of stars during the simulation time interval is shown in Fig. 23 and it is consistent with what was already shown in Fig. 20. The error components of the angular velocity estimated by the chord method are shown in Fig. 24. As previously discussed,

the x component reported in Fig. 24b is characterized by bigger errors than the y and z components. Indeed, the mean errors along the x, y, z axes are 0.0165 deg/s, 0.0475 deg/s, and -0.0182, respectively, whereas the standard deviations are 1.445 deg/s, 0.152 deg/s, and 0.116 deg/s. However, the magnitude of the errors are still consistent with the implementation of on-board filters to get at least a rough estimate of the angular velocity.

6. Conclusion

This paper presented some novel theoretical results related to the detected motion of the stars within the FOV of a star sensor in dynamic conditions. It has been shown that, when the satellite is experiencing a non-negligible angular velocity (in the paper it has been considered in the range 1-5 deg/s), the trajectories of the stars in the focal plane belong to conic section which features depend on the angles between the instantaneous rotation axis, the sensor line of sight (LOS) and the star direction. The outlined properties can be used to develop new techniques for the determination of the angular velocity from star sensor images. The proposed chord method represents a first attempt to use the discovered geometrical features for determining an approximated estimation of the angular velocity direction. The method is based on the computation of the intersection points between lines normal to the streaks left by the stars on the detector. Preliminary results have been obtained using a simplified numerical tool where the conics, the osculating circles and the normal lines have been evaluated without any source error. From these results, some generic characteristics of the method have been obtained. Finally, a high-fidelity star sensor simulator has been used to obtain the results of the chord method for a given angular velocity direction with the rate ranging from 1 to 5 deg/s. The numerical results are in agreement with the expected theoretical ones and demonstrate that the chord method can be used to get at least a first rough estimation of the angular velocity up to 5 deg/s.

References

[1] M. Paluszek, *Spacecraft attitude and orbit control*. Princeton Satellite Systems, Incorporated, 1996.

[2] F. L. Markley and J. L. Crassidis, *Fundamentals of spacecraft attitude determination and control*. Springer, 2014, vol. 33.

[3] H. Ma and S. Xu, "Magnetometer-only attitude and angular velocity filtering estimation for attitude changing spacecraft," *Acta Astronautica*, 2014. doi: 10.1016/j.actaastro.2014.05.002

[4] D. M. Gottlieb, "Star identification techniques," in *Spacecraft Attitude Determination and Control*, J. R. Wertz, Ed. Springer Netherlands, 2012, pp. 259–266. ISBN 9789400999077

[5] W. Zhang, W. Quan, and L. Guo, "Blurred star image processing for star sensors under dynamic conditions," *Sensors (Switzerland)*, 2012. doi: 10.3390/s120506712

[6] E. Gai, K. Daly, J. Harrison, and L. Lemos, "Star-sensor-based satellite attitude/attitude rate estimator," *Journal of Guidance, Control, and Dynamics*, 1985. doi: 10.2514/3.56393

[7] B. N. Agrawal and W. J. Palermo, "Angular rate estimation for Gyroless satellite attitude control," in *AIAA Guidance, Navigation, and Control Conference and Exhibit*, 2002. doi: 10.2514/6.2002-4463. ISBN 9781624101083

[8] M. Romano and B. N. Agrawal, "Evaluation of a gyroless spacecraft attitude estimation and control concept by numerical simulation and ground based experimentation," in *European Space Agency, (Special Publication) ESA SP*, 2003. ISSN 03796566

[9] D. Accardo and G. Rufino, "A procedure for three-dimensional angular velocity determination using a star sensor in high-rate rotation modes,"

in *Acta Astronautica*, 2001. doi: 10.1016/S0094-5765(01)00013-3. ISSN 00945765

[10] J. L. Crassidis, "Angular velocity determination directly from star tracker measurements," *Journal of Guidance, Control, and Dynamics*, vol. 25, no. 6, pp. 1165–1168, 2002. doi: 10.2514/2.4999

[11] C. C. Liebe, K. Gromov, and D. M. Meller, "Toward a stellar gyroscope for spacecraft attitude determination," *Journal of Guidance, Control, and Dynamics*, vol. 27, no. 1, pp. 91–99, 2004. doi: 10.2514/1.9289

[12] G. N. Rao, T. K. Alex, and M. S. Bhat, "Incremental-angle and angular velocity estimation using a star sensor," *Journal of Guidance, Control, and Dynamics*, 2002. doi: 10.2514/2.4928

[13] P. Singla, J. L. Crassidis, and J. L. Junkins, "Spacecraft angular rate estimation algorithms for star tracker-based attitude determination," in *Advances in the Astronautical Sciences*, 2003. ISSN 00653438

[14] S. Jo, Y. Choi, and H. Bang, "Optimal angular velocity estimation of spacecraft using only star tracker measurements," *Journal of Guidance, Control, and Dynamics*, 2015. doi: 10.2514/1.G000739

[15] G. Fasano, G. Rufino, D. Accardo, and M. Grassi, "Satellite angular velocity estimation based on star images and optical flow techniques," *Sensors*, vol. 13, no. 10, pp. 12 771–12 793, 2013. doi: 10.3390/s131012771

[16] X. Ning, Z. Ding, M. Xu, J. Fang, and G. Liu, "A Markley Variables-based Attitude Estimation Method Using Optical Flow and a Star Vector for Spinning Spacecraft," *Journal of Navigation*, 2018. doi: 10.1017/S0373463318000516

[17] M. Pal and M. S. Bhat, "Star sensor based spacecraft angular rate estimation independent of attitude determination," in *Proceedings of the IEEE International Conference on Control Applications*, 2013. doi: 10.1109/CCA.2013.6662812. ISBN 9781479915590

[18] T. Sun, F. Xing, X. Wang, J. Li, M. Wei, and Z. You, "Effective star tracking method based on optical flow analysis for star trackers," *Applied Optics*, 2016. doi: 10.1364/ao.55.010335

[19] Y. Tang, J. Li, and G. Wang, "Spacecraft angular velocity estimation algorithm for star tracker based on optical flow techniques," *Optical Engineering*, 2018. doi: 10.1117/1.oe.57.2.023101

[20] Z. Ding, X. Ning, and M. Gui, "Attitude Estimation Method for Spinning Spacecraft Using Markley Variables and Optical Flow of Stars," 2017. doi: 10.2991/iccia-17.2017.160

[21] J. Fisher and S. R. Vadali, "Gyroless attitude control of multi-body satellites using an unscented Kalman filter," in *Collection of Technical Papers - AIAA/AAS Astrodynamics Specialist Conference, 2006*, 2006. doi: 10.2514/6.2006-6163. ISBN 1563478226

[22] H. B. Liu, J. C. Yang, W. J. Yi, J. Q. Wang, J. K. Yang, X. J. Li, and J. C. Tan, "Angular velocity estimation from measurement vectors of star tracker," *Applied Optics*, 2012. doi: 10.1364/AO.51.003590

[23] C. Hajiyev, D. Cilden, and Y. Somov, "Gyro-free attitude and rate estimation for a small satellite using SVD and EKF," *Aerospace Science and Technology*, 2016. doi: 10.1016/j.ast.2016.06.004

[24] H. Leeghim, H. Bang, and C. Y. Lee, "Angular Rate and Alignment Estimation for Gyroless Spacecraft by Only Star Trackers," *International Journal of Control, Automation and Systems*, 2018. doi: 10.1007/s12555-017-0750-6

[25] F. Curti, D. Spiller, L. Ansalone, S. Becucci, D. Procopio, F. Boldrini, and P. Fidanzati, "Determining high rate angular velocity from star tracker measurements," in *Proceedings of the Internationa Astronautical Conference 2015*, 2015.

[26] F. Curti, D. Spiller, L. Ansalone, S. Becucci, D. Procopio, F. Boldrini, P. Fidanzati, and G. Sechi, "High angular rate determination algorithm

based on star sensing," *Advances in the Astronautical Sciences Guidance, Navigation and Control 2015*, vol. 154, p. 12, 2015.

[27] V. Schiattarella, D. Spiller, and F. Curti, "Star identification robust to angular rates and false objects with rolling shutter compensation," *Acta Astronautica*, 2019. doi: 10.1016/j.actaastro.2019.09.040

[28] V. Schiattarella, D. Spiller, and F. Curti, "Efficient star identification algorithm for nanosatellites in harsh environment," in *Advances in the Astronautical Sciences*, vol. 163, 2018, pp. 287–306.

[29] W. Burger and M. J. Burge, *Digital image processing: an algorithmic introduction using Java*. Springer London, 2016. ISBN 9781447166849

[30] H. Dorrie, *100 Great Problems of Elementary Mathematics: their history and solution*. Dover, 1965, ch. 55. ISBN 978-0486613482

[31] "StackExchange mathematics, origin-centred elliptical "spotlight" with conical light source of fixed aperture," https://math.stackexchange.com/questions/2351662/origin-centred-elliptical-spotlight-with-conical-light-source-of-fixed-apertur, accessed: 2020-01-31.

[32] K. Kendig, *Conics*. Cambridge University Press, 2005, no. 29.

[33] V. Schiattarella, D. Spiller, and F. Curti, "A novel star identification technique robust to high presence of false objects: The multi-poles algorithm," *Advances in Space Research*, vol. 59, no. 8, pp. 2133–2147, 2017. doi: 10.1016/j.asr.2017.01.034

[34] P. D. Wellner, "Adaptive thresholding for the digitaldesk - technical report EPC-1993-110," Rank Xerox Research Centre, Cambridge Laboratory, 61 Regent Street, Cambridge CB2 1AB, Tech. Rep., 1993.

[35] C. H. Messom, S. Demidenko, K. Subramaniam, and G. S. Gupta, "Size/position identification in real-time image processing using run length

encoding," in *IMTC/2002. Proceedings of the 19th IEEE Instrumentation and Measurement Technology Conference (IEEE Cat. No.00CH37276)*, vol. 2, May 2002. doi: 10.1109/IMTC.2002.1007101 pp. 1055–1059.

[36] L. Kazemi, J. Enright, and T. Dzamba, "Improving star tracker centroiding performance in dynamic imaging conditions," in *2015 IEEE Aerospace Conference*, March 2015. doi: 10.1109/AERO.2015.7119226 pp. 1–8.

[37] M. Sezgin and B. Sankur, "Survey over image thresholding techniques and quantitative performance evaluation," *Journal of Electronic imaging*, vol. 13, no. 1, pp. 146–166, 2004. doi: 10.1117/1.1631315

[38] R. Gonzalez and R. Woods, *Digital Image Processing.* Pearson/Prentice Hall, 2008. ISBN 9780131687288

[39] J. C. Dunlap, W. C. Porter, E. Bodegom, and R. Widenhorn, "Dark current in an active pixel complementary metal-oxide-semiconductor sensor," *Journal of Electronic Imaging*, vol. 20, no. 1, pp. 013 005–1/8, 2011. doi: 10.1117/1.3533328

[40] S. V. Vaseghi, *Advanced Digital Signal Processing and Noise Reduction.* John Wiley & Sons, 2008. ISBN 9780470740163. [Online]. Available: https://books.google.it/books?id=vVgLv0ed3cgC

[41] F. Boldrini, D. Procopio, S. Airy, and L. Giulicchi, "Miniaturised star tracker (aa-str) ready to fly," in *Proceedings of The 4S Symposium Small Satellites, Systems and Services*, vol. ESA SP-571, 2004, p. 46.